

Enhancing image quality prediction with self-supervised visual masking

Uğur Çoğalan
MPI Informatik
Germany
mbemana@mpi-inf.mpg.de

Hans-Peter Seidel
MPI Informatik
Germany
hpseidel@mpi-inf.mpg.de

Mojtaba Bemana
MPI Informatik
Germany
mbemana@mpi-inf.mpg.de

Karol Myszkowski
MPI Informatik
Germany
karol@mpi-inf.mpg.de

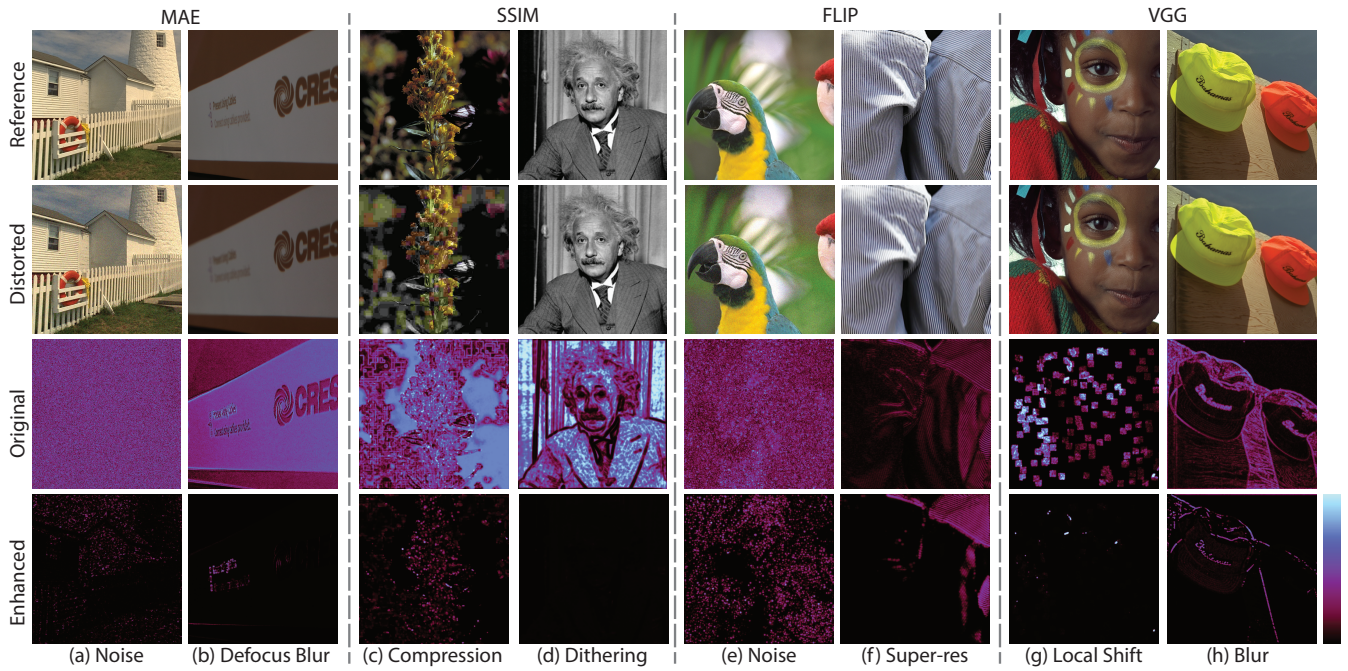


Figure 1: We introduce self-supervised visual masking that enhances image quality prediction for existing quality metrics such as MAE, SSIM, FLIP, and VGG. Our work is inspired by the well-known characteristic of the Human Visual System (HVS), visual masking, which results in locally varying sensitivity to image artifact visibility that reduces with increasing contrast magnitude of the original image pattern. We found that the learned masking clearly outperforms its traditional hand-crafted versions and better adapts to specific distortion patterns while remaining visually interpretable. In the first two rows, we show the reference and distorted images, while the third and fourth rows show the error maps as predicted by the original and our mask-enhanced metric versions. As can be seen, our mask-enhanced metrics better predict the local distortion visibility by the human observer. In the color scale, darker indicates lower errors.

ABSTRACT

Full-reference image quality metrics (FR-IQMs) aim to measure the visual differences between a pair of reference and distorted images, with the goal of accurately predicting human judgments. However, existing FR-IQMs, including traditional ones like PSNR and SSIM and even perceptual ones such as HDR-VDP, LPIPS, and DISTS, still fall short in capturing the complexities and nuances of human perception. In this work, rather than devising a novel IQM model, we seek to improve upon the perceptual quality of

existing FR-IQM methods. We achieve this by considering visual masking, an important characteristic of the human visual system that changes its sensitivity to distortions as a function of local image content. Specifically, for a given FR-IQM metric, we propose to predict a visual masking model that modulates reference and distorted images in a way that penalizes the visual errors based on their visibility. Since the ground truth visual masks are difficult to obtain, we demonstrate how they can be derived in a self-supervised manner solely based on mean opinion scores (MOS) collected from

an FR-IQM dataset. Our approach results in enhanced FR-IQM metrics that are more in line with human prediction both visually and quantitatively.

CCS CONCEPTS

• **Computing methodologies** → **Image quality metric.**

1 INTRODUCTION

Full-Reference Image Quality Metrics (FR-IQMs), which take as an input a pair of reference and distorted images, play a crucial role in a wide range of applications in digital image processing, such as image compression and transmission, as well as in evaluating the rendered content in computer graphics and vision. They are commonly used as a cost function in optimizing restoration tasks like denoising, deblurring, and super-resolution [Ding et al. 2021b]. Consequently, developing FR-IQMs that are accurately reflecting the visual quality of images in accordance with the characteristics of the human visual system (HVS) is critical. The most commonly used FR-IQMs for evaluating image quality are the mean square error (MSE) or mean absolute error (MAE). While these per-pixel metrics are easy to compute, they assess image quality regardless of spatial content, leading to false positive predictions. This can be seen in Fig. 1a, where noise is less noticeable in textured regions, while MAE predicts uniformly distributed error. Similarly, a depth-of-field blur is primarily visible on high-contrast fonts Fig. 1b, while MAE predicts the blur visibility also in smooth gradient regions. Other classic metrics like SSIM [Wang et al. 2004], while accounting for spatial content, often result in false positive predictions (the JPEG artifact and invisible color dithering pattern in Fig. 1c-d, respectively). A recent hand-crafted metric FLIP [Andersson et al. 2020] is specifically designed to predict the visual differences in time-sequential image-pair flipping, which can make it too sensitive for side-by-side image evaluation, e.g., noise less visible in high-contrast texture (Fig. 1e) and contrast reduction less visible in already high-contrast regions (Fig. 1f). Recognizing that hand-crafted image features may not adequately capture the HVS complexity, modern metrics [Zhang et al. 2018] strive to assess the perceptual dissimilarity between images by comparing deep features extracted from classification networks [Simonyan and Zisserman 2015]. These metrics appear to better account for the characteristics of the HVS; however, they are designed to generate a single value per image pair and can not provide correct error localization, as can be seen in Fig. 1g-h for the non-eccentricity pattern noise and Gaussian blur examples, respectively.

The objective of this work is not to develop a new perceptual FR-IQM; instead, we are interested in improving the quality prediction of existing metrics to align more closely with human judgment (Fig. 2). We also aim to enhance the accuracy of error map predictions by considering multiple factors such as image content, distortion levels, and distortion types. By detecting both the presence and evaluating the magnitude of visible distortion in each pixel, we aim to ensure that the metric predictions more accurately reflect the probability of a human observer detecting differences between a pair of images. In this regard, there have been several efforts toward incorporating the perceptual aspects of human vision, specifically visual masking [Legge and Foley 1980; Foley 1994; Wilson and

Gelb 1984], into FR-IQM methods [Lubin 1995; Daly 1993; Mantiuk et al. 2011, 2021]. In simple words, visual masking refers to the phenomenon in which certain parts of an image (in our application: distortions) may be less visible to the viewer due to the presence of other visual elements in the same image. Visual masking can affect image quality perception, making some image distortions less visible to the viewer [Ferwerda et al. 1997; Zeng et al. 2002]. However, existing visual masking models are typically hand-crafted and struggle to generalize effectively across various distortion types. Although learning a visual masking model appears to be a natural solution, the lack of reliable ground truth data for visual masking makes direct supervision impractical. In this work, we propose a self-supervised approach to predict visual masking using a dataset of images featuring a variety of distortions of different magnitudes whose quality has been evaluated in the mean opinion scores (MOS) experiment with human subjects [Lin et al. 2019]. In summary, our work offers the following contributions:

- We propose a lightweight CNN that generates a mask for a given reference and distorted input pair. The predicted mask acts as a per-pixel weight and, when multiplied with the inputs, greatly improves the performance of the existing FR-IQMs. The incorporation of our learned mask into any FR-IQM is seamless and demands minimal computational resources. While the CNN is trained specifically for each metric, it learns a generic masking model capable of identifying various types of distortions.
- We demonstrate that our masking model can be generalized to deep features and used as a per-layer feature map weight.
- Our solution significantly enhances the accuracy of quality prediction for FR-IQMs across various test datasets. Furthermore, it produces per-pixel error maps that visually align more closely with human perception compared to the original FR-IQMs.

We will make our code publicly available upon the paper’s acceptance.

2 PREVIOUS WORK

FR-IQMs can be categorized into classical metrics, which perform the computation directly in the image space, and learning-based metrics, which leverage deep feature models to assess image quality.

Classic metrics Basic FR-IQMs, such as MSE, RMSE, and MAE, compute the per-pixel difference to quantify image distortion. While these metrics are straightforward to calculate, their consistency with human vision is typically low. Such perceptual consistency can be improved by considering a relative error, instead of its absolute measure, as in PSNR and the symmetric mean absolute percentage error (SMAPE) [Vogels et al. 2018]. To account for the spatial aspects of the HVS, alternative metrics such as SSIM [Wang et al. 2004] are introduced, which consider image patches and measure local differences in luminance, contrast, and structural information. SSIM is further extended to multi-scale MS-SSIM [Wang et al. 2003] and complex wavelet CW-SSIM [Sampat et al. 2009] versions that capture both global and local structural information. FSIM [Zhang et al. 2011] decomposes the image into multiple subbands using Gabor filters and compares subband responses between the reference and distorted images. By assuming that natural images have a

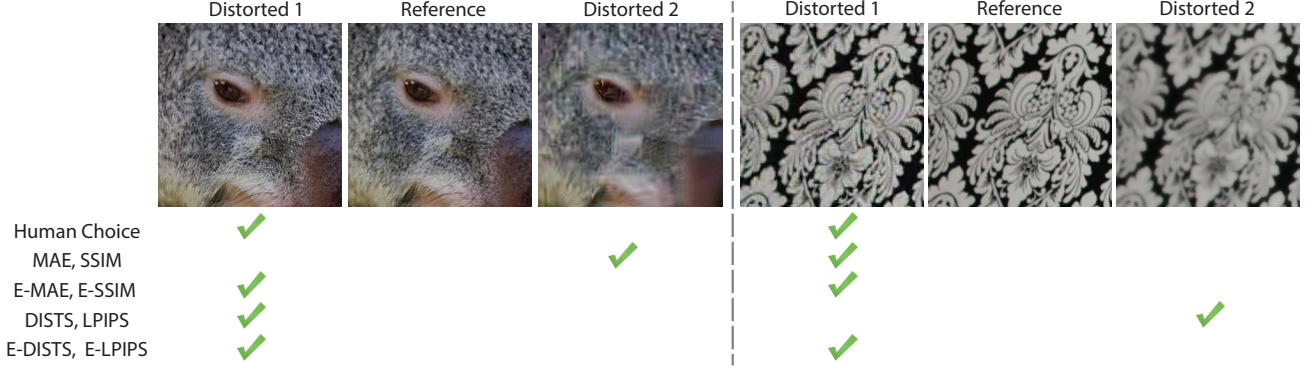


Figure 2: Agreement of metric predictions with human judgments. We consider the classic (MAE and SSIM) and learning-based (LPIPS and DISTs) metrics, and we compare their prediction to their enhanced versions (E-MAE, E-SSIM, E-DISTS, and E-LPIPS) using our approach. On the left, we see a situation where MAE and SSIM favor JPEG-like artifacts over slightly resampled textures. On the right, we encounter a scenario where LPIPS and DISTs prefer blur over a subtle color shift. Our extended metric versions are always aligned with human choice. The images have been extracted from the PIPAL dataset [Gu et al. 2020].

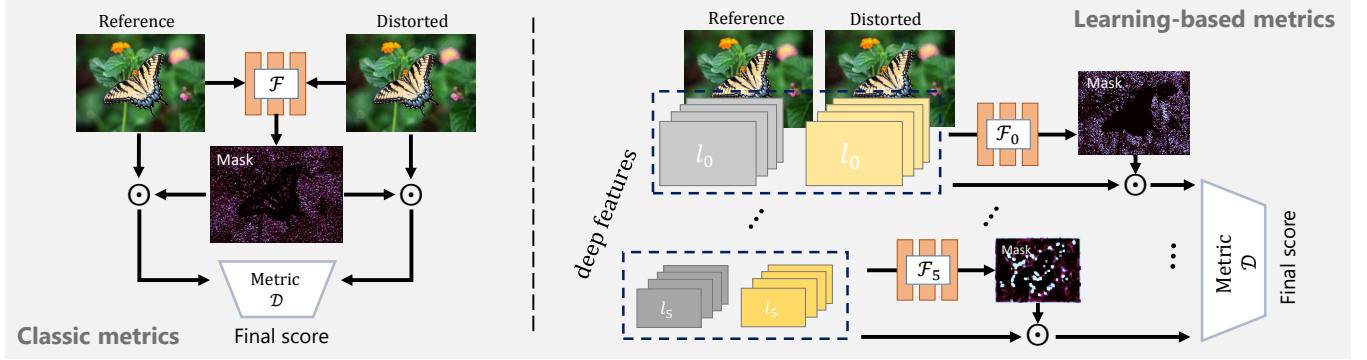


Figure 3: Our proposed visual masking approach for enhancing classic metrics such as MAE and SSIM (left) and learning-based metrics such as DISTs or LPIPS (right). For classic metrics, the input to our mask predictor network \mathcal{F} are sRGB images, while for learning-based metrics, the inputs are the VGG features extracted from the images. We learn the visual masks in a self-supervised fashion by minimizing the difference between the metric final score and human scores collected from an FR-IQM dataset.

specific distribution of pixel values, models based on information theory [Sheikh and Bovik 2005, 2006] measure the mutual information between images by comparing their joint histograms and taking into account the statistical dependencies between neighboring pixels. Classical metrics can offer either a single overall quality score or a visibility map indicating the distortion intensity. VDM [Lubin 1995], VDP [Daly 1993], and HDR-VDP [Mantiuk et al. 2011, 2021] measure either the visibility of distortions or perceived distortions magnitude, or both by considering various visual aspects such as luminance adaptation, contrast sensitivity, and visual masking. A more recent metric, FLIP [Andersson et al. 2020], emphasizes color differences, and it is sensitive to even subtle distortions by emulating flipping between the compared image pair.

Deep learning-based metrics In recent years, research in FR-IQA has been placing greater emphasis on perceptual comparisons in deep feature space rather than image space to enhance the alignment with human judgments. Prashnani et al. [2018] are among the first to utilize deep feature models learned from human-labeled data to predict perceptual errors. However, Zhang et al. [2018]

demonstrate that internal image representations from classification networks can be used for image comparison. They propose the Perceptual Image Patch Similarity (LPIPS) index, which quantifies image similarity by measuring the ℓ_2 distances between pre-trained VGG features. To further improve the correlation with human judgments, they learn per-channel weights for selected VGG features using their collected perceptual similarity dataset. Recognizing that simple ℓ_p -norm measures fail to consider the statistical dependency of errors across different locations, Ding et al. [2020] introduce the DISTs, which aims to measure the texture and structure similarity between feature pairs by comparing their global mean, variance, and correlations in the form of SSIM. Building upon this work, A-DISTS [Ding et al. 2021a] extended the approach to incorporate local structure and texture comparisons. Moving away from deterministic point-wise feature comparisons, DeepWSD [Liao et al. 2022] compares the overall distributions of features using the Wasserstein distance, a statistical measure for comparing two distributions. Nevertheless, the majority of the proposed IQMs metrics are targeted toward producing a single quality score and are not primarily

designed to generate per-pixel error maps. In this regard, Wolski et al. [2018] employ a custom CNN model trained in a fully supervised way using coarse user marking data to predict an error visibility map that highlights the regions where distortions are more likely to be noticeable.

In this work, we extend the classic and deep learning-based metrics by introducing a learnable component trained on perceptual MOS data in a self-supervised way. By implicitly analyzing local image content, our model derives per-pixel maps which mimic visual masking, effectively modeling the visual significance of distortions.

3 SELF-SUPERVISED VISUAL MASKING

In this section, we elaborate on our methodology for perceptually calibrating the existing FR-IQMs. Given a reference and distorted pair $(X \text{ and } Y) \in \mathbb{R}^{H \times W \times C}$, we first learn a visual mask, $M \in \mathbb{R}^{H \times W \times 1}$, which has the same spatial dimensions as the inputs. For classical metrics (Fig. 3-left), the input X and Y are sRGB images ($C = 3$), while for learning-based metrics such as LPIPS or DISTs, the inputs are the VGG features extracted from the images and C is the number of channels in a given VGG layer (Fig. 3-right). The predicted mask is then element-wised multiplied with the X and Y before being fed into an FR quality metric, \mathcal{D} . Note that the same mask is applied to both the reference and distorted inputs. For estimating the mask M , we utilize a lightweight CNN denoted as \mathcal{F} , which takes both X and Y as input. Mathematically, this can be expressed as:

$$M = \mathcal{F}(X, Y) \quad (1)$$

It is important to note that the network \mathcal{F} is trained specifically for a metric \mathcal{D} . In the case of metrics such as LPIPS and DISTs, we follow their specific architecture and compute a mask for each layer using a separate \mathcal{F} , and the same mask is applied for all channels in a given layer (Fig. 3-right). Since we cannot directly supervise the output of the mask generator network, we adopt a self-supervised approach to train it using an IQM dataset with a single quality score. The network’s parameters are optimized by minimizing the ℓ_2 difference between the metric output value and human scores. Our loss is formulated as follows:

$$Loss = \|\mathcal{G}(\mathcal{D}(M \odot X, M \odot Y)) - q\|_2^2 \quad (2)$$

Here, $q \in [0, 1]$ represents the normalized mean opinion score when comparing the images X and Y . As the metric response can vary in an arbitrary range, following a similar approach in Zhang et al. [2018], a small network \mathcal{G} is jointly trained to map the metric response to the human ratings. Note that the network \mathcal{G} is not applied during inference time but rather during the training process.

3.1 Training and network details

For training, we use the KADID dataset [Lin et al. 2019], which comprises 81 natural images that have been distorted using 25 types of traditional distortions, each at five different levels, making roughly 10k training pairs. Note that we train our mask generator network \mathcal{F} for all the distortion categories together rather than for one specific category. We find that a simple CNN with three convolutional layers, each consisting of 64 channels, suffices for successful training. ReLU activation is applied after each layer, while we use Sigmoid activation for the final layer to keep the mask values

in the range between 0 and 1. Our mapping network \mathcal{G} consists of two 32-channel fully connected (FC) ReLU layers, followed by a 1-channel FC layer with Sigmoid activation. The batch size for training is set to 4. We employ the Adam optimizer [Kingma and Ba 2017] with an initial learning rate of 10^{-4} and a weight decay of 10^{-6} .

Table 1: Performance comparison of existing FR-IQMs (top part) and their enhanced versions using our approach (specified by the prefix E in the bottom part) on three standard IQM datasets. Higher values of SRCC, PLCC, and KRCC indicate better quality prediction. The first and second best metrics for each dataset are indicated in bold and underlined, respectively. Additionally, the version with superior correlation is highlighted in dark gray for each metric.

Metric	CSIQ			TID			PIPAL		
	PLCC	SRCC	KRCC	PLCC	SRCC	KRCC	PLCC	SRCC	KRCC
FSIM	0.900	0.913	0.740	0.847	0.789	0.611	0.651	0.617	0.441
VIF	0.826	0.841	0.642	0.820	0.813	0.616	0.584	0.538	0.378
HDR-VDP-2	0.912	0.815	0.724	0.815	0.775	0.588	0.592	0.514	0.363
PieAPP	0.827	0.840	0.653	0.832	0.849	0.652	0.729	0.709	0.521
MAE	0.819	0.801	0.599	0.639	0.627	0.409	0.458	0.443	0.304
E-MAE	0.871	0.917	0.738	0.857	0.863	0.673	0.597	0.606	0.429
PSNR	0.851	0.837	0.645	0.726	0.714	0.540	0.468	0.456	0.314
E-PSNR	0.901	0.910	0.728	0.855	0.844	0.656	0.637	0.629	0.446
SSIM	0.848	0.863	0.665	0.697	0.663	0.479	0.550	0.534	0.373
E-SSIM	0.869	0.910	0.732	0.842	0.868	0.677	0.671	0.656	0.469
MS-SSIM	0.826	0.841	0.642	0.820	0.813	0.616	0.584	0.538	0.379
E-MS-SSIM	0.862	0.895	0.709	0.806	0.825	0.621	0.642	0.634	0.453
FLIP	0.731	0.724	0.527	0.591	0.537	0.413	0.498	0.442	0.306
E-FLIP	0.871	0.902	0.715	0.859	0.858	0.666	0.621	0.612	0.434
VGG	0.938	0.952	0.804	0.853	0.820	0.639	0.643	0.610	0.432
E-VGG	0.914	0.938	0.776	0.895	0.889	0.710	0.695	0.675	0.485
LPIPS	0.944	0.929	0.769	0.803	0.756	0.568	0.640	0.598	0.424
E-LPIPS	0.922	0.933	0.771	0.884	0.876	0.689	0.705	0.678	0.490
DISTS	0.947	0.947	0.796	0.839	0.811	0.619	0.645	0.626	0.445
E-DISTS	0.932	0.925	0.753	0.903	0.915	0.725	0.725	0.697	0.507
DeepWSD	0.949	0.961	0.821	0.879	0.861	0.674	0.593	0.584	0.409
E-DeepWSD	0.937	0.937	0.775	0.905	0.892	0.710	0.704	0.672	0.485

4 RESULTS

In this section, we first present our experimental setup, which we use then for our method evaluation and ablations of different training strategies.

4.1 Experimental setup

We employ our visual masking approach to enhance some of the classical metrics (MAR, PSNR, SSIM, MS-SSIM, and FLIP) and recent learning-based methods (VGG, LPIPS, DISTs, and DeepWSD). Note for MS-SSIM, we used the same \mathcal{F} across all scales, while the inputs are images at different scales. Moreover, the metric called VGG is computed by simply taking the ℓ_1 difference between VGG features for the same layers as originally chosen for LPIPS and DISTs. We assess the performance of our proposed approach on three well-established IQM datasets, including CSIQ [Larson and

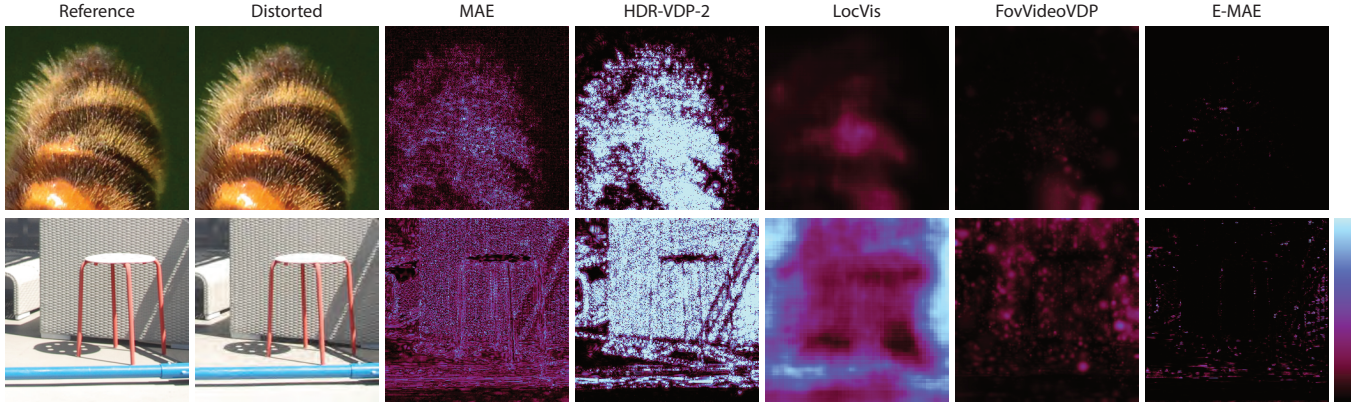


Figure 4: The visual comparisons of distortion visibility maps for superresolution (upper row) and joint denoising and superresolution (bottom row) tasks as acquired from the PIPAL dataset. The first two columns present the reference and distorted images, followed by the respective metric predictions: MAE, HDR-VDP-2 [Mantiuk et al. 2011], LocVis [Wolski et al. 2018], FovVideoVDP [Mantiuk et al. 2021], and our E-MAE. As can be seen, the existing metrics tend to overestimate the distortion visibility. Note that LocVis and E-MAE have not seen such distortions in their training.

Chandler 2010], TID2013 [Ponomarenko et al. 2015], and PIPAL [Gu et al. 2020]. The first two datasets mainly consist of synthetic distortions, ranging from 1k to 3k images. On the other hand, PIPAL is the most comprehensive IQA dataset due to its diverse and complex distortions, consisting of 23k images. Each reference image in this dataset was subjected to 116 distortions, including 19 GAN-type distortions. For evaluation, following Ding et al. [2020], we resize the smaller side resolution of input images to 224 while maintaining the aspect ratio. For each dataset, three metrics are used for evaluation: Spearman’s rank correlation coefficient (SRCC), Pearson linear correlation coefficient (PLCC), and the Kendall rank correlation coefficient (KRCC). The PLCC measures the accuracy of the predictions, while the SRCC indicates the monotonicity of the predictions, and the KRCC measures the ordinal association. When computing the PLCC, we mapped the metric scores to the MOS values using a four-parameter function [Ding et al. 2020].

4.2 Evaluations

In this section, we present the outcome of the quantitative (agreement with the MOS data) and qualitative (the quality of error maps) evaluation of our method. We also analyze the mask content and relate it with perceptual models of contrast and blur perception. Finally, we analyze the error map prediction of different distortion levels, and we consider the potential use of our enhanced E-MAE metric as a loss in an image restoration task.

Quality prediction The experimental results are presented in Tbl. 1, where with the prefix E, we denote our proposed extension for each specific IQM. Our extension of traditional metrics, such as MAE, PSNR, SSIM, and FLIP consistently improves their performance for all datasets. This is remarkable as those metrics are commonly used, and our simple extension can make their distortion prediction closer to the human observer. Interestingly, the enhanced E-MAE and E-PSNR outperform recent learning-based VGG, LPIPS, and DISTS in the TID dataset while showing a comparable performance for the PIPAL dataset. Notable improvements are also observed in both datasets for the recent learning-based

metrics (E-VGG, E-LPIPS, E-DIST, and E-DeepWSD), positioning them at a level comparable to other state-of-the-art IQMs, such as PieAPP [Prashnani et al. 2018]. The only exception is the case of the small-scale CSIQ dataset, where the original learning-based metrics achieve high correlations with the MOS data and leave little space for further improvements.

Error map prediction In Fig. 1, we show the error maps predicted by various existing IQMs and their enhanced versions for a set of images featuring different types of distortions. Note that the error map for VGG is visualized for the first layer. Moreover, the scores for MAE and VGG metrics exist in an unbounded range, and following Andersson et al. [2020], we apply a Sigmoid function to normalize them within the range from zero to one. Fig. 11 presents more examples for the SSIM and VGG metrics. Additionally, Fig. 4 showcases two examples where our E-MAE metric achieves more visually accurate error maps compared to well-established visibility metrics such as HDR-VDP-2 [Mantiuk et al. 2011], LocVis [Wolski et al. 2018], and FovVideoVDP [Mantiuk et al. 2021]. Please refer to our supplementary material for more comprehensive results.

Mask visualization It is also intriguing to see the learned mask, i.e., the output of the network \mathcal{F} , and to compare it with a traditional visual contrast masking model, such as the one used in JPEG2000 compression [Zeng et al. 2002]. To this end, Fig. 5 presents our masks generated for noise and blur distortions. We consider the same distortion level and three levels of image contrast enhancement ($\times 0.5$, $\times 1$, and $\times 2$). In the case of noise distortion, our learned masks predict stronger visual masking in the high-contrast butterfly and better noise visibility in the out-of-focus smooth background. Increasing image contrast ($\times 2$) leads to even stronger visual masking in the butterfly area and the plant behind it. Reducing image contrast ($\times 0.5$) leads to the inverse effect. Such behavior is compatible with the visual contrast masking model [Zeng et al. 2002; Tur-sun et al. 2019], where due to self-contrast masking, the higher the contrast of the original signal (e.g., on edges), the stronger the distortion should be to make it visible. Along a similar line,



Figure 5: Comparison of our E-MAE metric masks for the noise (fifth row) and blur (sixth row) distortions as a function of different image contrast ($\times 0.5$, $\times 1$, and $\times 2$). In the fourth row, we also show a map with the human sensitivity to local contrast changes as predicted by a traditional model of visual contrast masking [Tursun et al. 2019, Eq.4]. In all cases, darker means less sensitive. However, the scale of our masks that serve as weights in the E-MAE metric is different than the one for the visual contrast masking model that directly denotes the hypothetical HVS response to local distortion contrast.

due to neighborhood masking, the higher the contrast texture, the stronger the visual masking as well. In the case of blur distortion, our learned mask predicts its strong visibility on high-contrast edges. The stronger the image contrast ($\times 2$), the blur visibility improves. Assigning a higher weight by our mask to high contrast regions agrees with perceptual models of blur detection and discrimination [Watson and Ahumada 2011; Sebastian et al. 2015]. Note that we derive each mask taking as an input both the reference and distorted images; the mask can resolve even per-pixel distortions, as in the case of noise (Fig. 5), and accordingly informs the E-MAE metric on the perceptual importance of such distortions. What is also remarkable is that the HVS might impose contradictory requirements on hand-crafted visual models that become specific for a

given distortion. This is well illustrated in Fig. 5, where noise can be better masked by strong contrast patterns [Zeng et al. 2002; Tursun et al. 2019] while blur is actually better revealed by strong contrast patterns [Watson and Ahumada 2011]. Our learned E-MAE mask somehow recognizes the distortion context and reacts as expected by penalizing less noise distortion in high-contrast and textured regions while penalizing more blur distortion at high-contrast edges. Interestingly, such local, seemingly contradictory behavior has been learned solemnly by providing multiple pairs of reference and distortion images along with the corresponding quality MOS rating which is just a single number. No annotation on specific distortion types has been required in our training. Fig. 8 shows further examples that our learned masking is also informed about contrast masking by texture [Ferwerda et al. 1997] and the contrast sensitivity function (CSF) [Daly 1993; Barten 1999; Wuerger et al. 2020].

Sensitivity to different distortion levels Our predicted mask can effectively highlight both the presence of a perceived error between two images at each pixel as well its corresponding magnitude. In this regard, Fig. 9 illustrates the predicted mask for a set of Monte Carlo-rendered images with a progressively increased number of samples per pixel (SPP). As can be seen, the perceived error decreases as the sample count rises, which is better reflected in our predicted Mask and the E-MAE error map compared to the MAE metric. Note that the predicted mask correctly reacts to the emergence of new fireflies as the sample count increases.

Employing the enhanced metric as the loss In this part, we investigate the benefit of the enhanced IQM metrics in optimizing image restoration algorithms. To this end, we employ MAE and E-MAE as loss functions for training image denoising using the state-of-the-art image restoration method, Restormer [Zamir et al. 2022]. For our training set, we select the images in the BSD400 dataset [Martin et al. 2001] and introduce synthetic noise to these images by applying additive white Gaussian noise with a randomly chosen standard deviation ranging between 0 and 50. Then, we evaluate the trained models on five benchmark datasets, consistent with the ones used in [Zamir et al. 2022]. We conduct our evaluation for various noise levels and report the results in Tbl. 2. We can observe that training with MAE leads to a higher PSNR value; however, training with E-MAE yields better scores when assessing with LPIPS and E-MAE metrics. The visual results are provided in Fig. 10.

4.3 Ablations

We perform a set of ablations to investigate the impact of reduced training data in terms of distortion levels, reference image number, and distortion type diversity on the E-MAE metric prediction accuracy.

Distortion levels The first experiment analyzes the importance of incorporating various distortion levels into our training set. In this regard, we train our network for the E-MAE metric using only one distortion level per category, and the results are reported in Fig. 6. Interestingly, for all the datasets (except PIPAL), an inverse U-shape trend emerged across five different distortion levels, where we observe the lowest correlation when training with the minimum and maximum distortion levels (levels 1 and 5). Conversely, a

Table 2: Evaluation of a blind Gaussian denoising task when employing MAE and our E-MAE as loss functions. We assess the performance on synthetic datasets created with four distinct noise levels (σ).

Loss	$\sigma = 15$				$\sigma = 25$				$\sigma = 50$				$\sigma = 60$			
	PSNR \uparrow	SSIM \uparrow	LPIPS \downarrow	E-MAE \downarrow	PSNR \uparrow	SSIM \uparrow	LPIPS \downarrow	E-MAE \downarrow	PSNR \uparrow	SSIM \uparrow	LPIPS \downarrow	E-MAE \downarrow	PSNR \uparrow	SSIM \uparrow	LPIPS \downarrow	E-MAE \downarrow
MAE	34.38	0.94	0.056	0.0341	31.92	0.90	0.091	0.0847	28.77	0.83	0.163	0.320	27.97	0.81	0.179	0.429
E-MAE	34.05	0.94	0.057	0.0320	31.50	0.90	0.090	0.0722	28.04	0.83	0.159	0.227	27.12	0.80	0.177	0.294

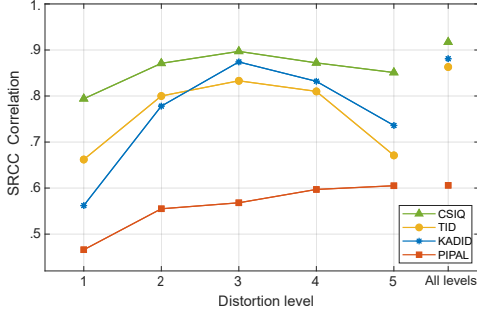


Figure 6: Evaluation of E-MAE training performance using only selected distortion levels for each distortion category. We measure the SRCC correlation with the MOS data, and as a reference, we also include the results of complete training with all distortion levels.

moderate amount of distortion (level 3) appears to be sufficiently representative for each distortion category and achieved a comparable correlation to training with all five levels. This behavior can be anticipated because, at the lowest and highest distortion levels, the distortions are either barely visible or strongly visible, leading to the consistent selection of mostly extreme rating scores. Consequently, when the network is exclusively exposed to images with one such extreme distortion and rating levels, it fails to learn to differentiate between them. On the other hand, at moderate distortion levels where distortions are partially visible or invisible, the network has a better opportunity to learn masks that behave differently for varying spatial locations.

Dataset size Although we employ a large-scale KADID dataset in our training (25 distortion types \times 5 distortion levels), the number of reference images is limited to 81. This ablation aims to investigate the training performance by even further reducing the number of reference images. To this end, we perform multiple runs of E-MAE metric training using randomly selected subsets of 20, 40, and 60 reference images. Fig. 7 presents the SRCC correlations averaged over multiple runs. The correlation differences between 40, 60, and the full set of 81 reference images are minor. In the case of 20 reference images, the performance is slightly lower and the variance higher, which indicates that 20 scenes might not be enough to capture image content variability.

Distortion diversity We investigate the impact of separate E-MAE training on specific distortion subsets such as noise, blur, combined noise and blur, as well as the complete KADID dataset. At the test time, we evaluate trained this way E-MAE versions on noise and blur subsets of the TID dataset, as well as its complete version. The results, presented in Tbl. 3, reveal that training

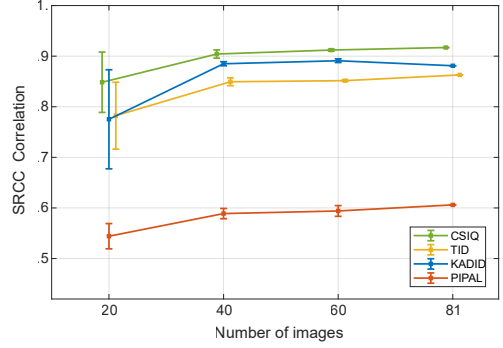


Figure 7: Evaluation of E-MAE training performance using different numbers of the reference images (scenes). Multiple training runs have been performed for 20, 40, and 60 randomly selected scenes from the full set of 81 reference images. The data points represent the respective SRCC correlation averages over such runs, while the vertical bars depict the standard deviation.

Table 3: The SRCC correlation with the MOS data for the E-MAE metric trained with specific distortion categories (noise, blur, noise&blur) and the entire (all) KADID dataset, as indicated in the brackets. The TID dataset is used for testing, where the “Category” columns indicate whether only the noise and blur subsets are considered or the entire dataset.

Metric	Category: noise	blur	all
MAE	0.601	0.934	0.545
E-MAE (noise)	0.847	0.927	0.674
E-MAE (blur)	0.732	0.926	0.655
E-MAE (noise & blur)	0.841	0.936	0.726
E-MAE (all)	0.906	0.955	0.857

solely on the noise category unsurprisingly improves the SRCC correlation within that category; however, it also enhances the overall correlation for the TID dataset with respect to the original MAE. Conversely, training exclusively on blur does not improve the performance within the blur category itself, as the blur distortion already exhibits a strong correlation (0.934) for the MAE metric, making any improvement marginal. On the other hand, we noticed that training with all categories combined significantly improves the correlation in both the noise and blur categories compared to training with only noise or blur categories, which can suggest that exposing the network to a wider range of distortion types enables better generalization.

5 LIMITATIONS

The actual visual contrast masking is the function of the viewing condition and the display size [Chandler 2013], which is often considered in the perceptual quality metrics [Daly 1993; Mantiuk et al. 2011, 2021; Andersson et al. 2020] but otherwise mostly ignored. However, the effectiveness of our visual masking model is limited to the experimental setup where human scores are obtained in the KADID dataset. As shown in Fig. 8, in the context of the CSF reproduction, our metric might not be well calibrated for near contrast threshold stimuli, whose visibility is also affected by the viewing distance and display conditions. Improving on those aspects, we relegate to future work.

6 CONCLUSION

In this paper, we present a new approach towards reducing the notorious gap between the existing quality metric prediction and the actual distortion visibility by the human observer. We achieve this by self-supervised training of a metric-specific network using the existing distortion datasets labeled with mean opinion score (MOS). We show that although overall image quality is rated with a single MOS value in the training data, by securing sufficient diversity of such training, as detailed in our ablation study, the network can leverage global MOS into a meaningful per-pixel mask. The mask, through different weighting of local distortion visibility, helps a given metric to aggregate such local information into the comprehensive MOS value, as imposed by the training data. The mask can be learned directly in the image space for traditional metrics or in the feature space for recent learning-based metrics. In either case, it is trivial to incorporate into the existing metrics. Remarkably, our approach improves the performance of commonly used metrics, such as MAE, PSNR, SSIM, and FLIP on all datasets we tested. The prediction accuracy of recent learning-based metrics is typically substantially enhanced.

REFERENCES

- Pontus Andersson, Jim Nilsson, Tomas Akenine-Möller, Magnus Oskarsson, Kalle Åström, and Mark D. Fairchild. 2020. FLIP: A Difference Evaluator for Alternating Images. *Proceedings of the ACM on Computer Graphics and Interactive Techniques* 3, 2 (2020), 15:1–15:23. <https://doi.org/10.1145/3406183>
- Peter G.J. Barten. 1999. *Contrast sensitivity of the human eye and its effects on image quality*. SPIE – The International Society for Optical Engineering. <https://doi.org/10.1117/3.353254>
- Martin Čadík, Robert Herzog, Rafał Mantiuk, Radosław Mantiuk, Karol Myszkowski, and Hans-Peter Seidel. 2013. Learning to predict localized distortions in rendered images. In *Computer Graphics Forum*, Vol. 32. Wiley Online Library, 401–410.
- Damon M Chandler. 2013. Seven challenges in image quality assessment: past, present, and future research. *International Scholarly Research Notices* 2013 (2013).
- S. Daly. 1993. The Visible Differences Predictor: An Algorithm for the Assessment of Image Fidelity. In *Digital Image and Human Vision*. 179–206.
- Keyan Ding, Yi Liu, Xueyi Zou, Shiqi Wang, and Kede Ma. 2021a. Locally Adaptive Structure and Texture Similarity for Image Quality Assessment. In *Proceedings of the 29th ACM International Conference on Multimedia*. ACM. <https://doi.org/10.1145/3474085.3475419>
- Keyan Ding, Kede Ma, Shiqi Wang, and Eero P. Simoncelli. 2020. Image Quality Assessment: Unifying Structure and Texture Similarity. *CoRR abs/2004.07728* (2020). [arXiv:2004.07728](https://arxiv.org/abs/2004.07728) <https://arxiv.org/abs/2004.07728>
- Keyan Ding, Kede Ma, Shiqi Wang, and Eero P Simoncelli. 2021b. Comparison of full-reference image quality models for optimization of image processing systems. *International Journal of Computer Vision* 129 (2021), 1258–1281.
- James A Ferwerda, Peter Shirley, Sumanta N Pattanaik, and Donald P Greenberg. 1997. A model of visual masking for computer graphics. In *Proceedings of the 24th annual conference on Computer graphics and interactive techniques*. 143–152.
- Arthur Firmino, Jeppe Revall Frisvad, and Henrik Wann Jensen. 2022. Progressive Denoising of Monte Carlo Rendered Images. In *Computer Graphics Forum*, Vol. 41. Wiley Online Library, 1–11.
- J.M. Foley. 1994. Human luminance pattern-vision mechanisms: masking experiments require a new model. *J. Opt. Soc. Am. A* 11, 6 (1994), 1710–19.
- Jinjin Gu, Haoming Cai, Haoyu Chen, Xiaoxing Ye, Jimmy Ren, and Chao Dong. 2020. PIPAL: a Large-Scale Image Quality Assessment Dataset for Perceptual Image Restoration. *arXiv:2007.12142* [eess.IV]
- Diederik P. Kingma and Jimmy Ba. 2017. Adam: A Method for Stochastic Optimization. *arXiv:1412.6980* [cs.LG]
- Eric C. Larson and Damon M. Chandler. 2010. Most apparent distortion: full-reference image quality assessment and the role of strategy. *J. Electronic Imaging* 19 (2010), 011006.
- Gordon E. Legge and John M. Foley. 1980. Contrast masking in human vision. *J. Opt. Soc. Am.* 70, 12 (1980), 1458–1471.
- Xingran Liao, Baoliang Chen, Hanwei Zhu, Shiqi Wang, Mingliang Zhou, and Sam Kwong. 2022. DeepWSD: Projecting Degradations in Perceptual Space to Wasserstein Distance in Deep Feature Space. In *Proceedings of the 30th ACM International Conference on Multimedia*. ACM. <https://doi.org/10.1145/3503161.3548193>
- Hanhe Lin, Vlad Hosu, and Dietmar Saupe. 2019. KADID-10k: A Large-scale Artificially Distorted IQA Database. In *2019 Eleventh International Conference on Quality of Multimedia Experience (QoMEX)*. 1–3. <https://doi.org/10.1109/QoMEX.2019.8743252>
- J. Lubin. 1995. A visual discrimination model for imaging system design and development. In *Vision models for target detection and recognition*, Peli E. (Ed.). World Scientific, 245–283.
- Rafał Mantiuk, Kil Joong Kim, Allan G Rempel, and Wolfgang Heidrich. 2011. HDR-VDP-2: A calibrated visual metric for visibility and quality predictions in all luminance conditions. *ACM Transactions on graphics (TOG)* 30, 4 (2011), 1–14.
- Rafał K Mantiuk, Gyorgy Denes, Alexandre Chapiro, Anton Kaplanyan, Gizem Rufo, Romain Bachy, Trisha Lian, and Anjul Patney. 2021. FovVideoVDP: A visible difference predictor for wide field-of-view video. *ACM Transactions on Graphics (TOG)* 40, 4 (2021), 1–19.
- D. Martin, C. Fowlkes, D. Tal, and J. Malik. 2001. A Database of Human Segmented Natural Images and its Application to Evaluating Segmentation Algorithms and Measuring Ecological Statistics. In *Proc. 8th Int'l Conf. Computer Vision*, Vol. 2. 416–423.
- Nikolay Ponomarenko, Lina Jin, Oleg Ieremeiev, Vladimir Lukin, Karen Egiazarian, Jaakko Astola, Benoit Vozel, Kacem Chehdi, Marco Carli, Federica Battisti, and C.-C. Jay Kuo. 2015. Image database TID2013: Peculiarities, results and perspectives. *Signal Processing: Image Communication* 30 (2015), 57–77. <https://doi.org/10.1016/j.image.2014.10.009>
- Ekta Prashnani, Hong Cai, Yasamin Mostofi, and Pradeep Sen. 2018. Pieapp: Perceptual image-error assessment through pairwise preference. In *Proceedings of the IEEE Conference on Computer Vision and Pattern Recognition*. 1808–1817.
- Mehul P. Sampat, Zhou Wang, Shalini Gupta, Alan Conrad Bovik, and Mia K. Markey. 2009. Complex Wavelet Structural Similarity: A New Image Similarity Index. *IEEE Transactions on Image Processing* 18, 11 (2009), 2385–2401.
- Stephen Sebastian, Johannes Burge, and Wilson S. Geisler. 2015. Defocus blur discrimination in natural images with natural optics. *Journal of Vision* 15, 5 (04 2015), 16–16.
- H.R. Sheikh and A.C. Bovik. 2006. Image information and visual quality. *IEEE Transactions on Image Processing* 15, 2 (2006), 430–444. <https://doi.org/10.1109/TIP.2005.859378>
- Hamid R Sheikh and Alan C Bovik. 2005. Information embedded in images: Joint estimation of information and distortion. In *Proceedings of the IEEE International Conference on Image Processing*, Vol. 2. IEEE, II–702.
- Karen Simonyan and Andrew Zisserman. 2015. Very Deep Convolutional Networks for Large-Scale Image Recognition. *arXiv:1409.1556* [cs.CV]
- Cara Tursun, Elena Arabadzhiyska-Koleva, Marek Wernikowski, Radosław Mantiuk, Hans-Peter Seidel, Karol Myszkowski, and Piotr Didyk. 2019. Luminance-Contrast-Aware Foveated Rendering. *ACM Trans. Graph.* 38, 4, Article 98 (2019).
- Thijs Vogels, Fabrice Rousselle, Brian McWilliams, Gerhard Rothlin, Alex Harvill, David Adler, Mark Meyer, and Jan Novák. 2018. Denoising with kernel prediction and asymmetric loss functions. *ACM Transactions on Graphics (TOG)* 37, 4 (2018), 1–15.
- Zhou Wang, A.C. Bovik, H.R. Sheikh, and E.P. Simoncelli. 2004. Image quality assessment: from error visibility to structural similarity. *IEEE Transactions on Image Processing* 13, 4 (2004), 600–612. <https://doi.org/10.1109/TIP.2003.819861>
- Z. Wang, E.P. Simoncelli, and A.C. Bovik. 2003. Multiscale structural similarity for image quality assessment. In *The Thirty-Seventh Asilomar Conference on Signals, Systems & Computers*, 2003, Vol. 2. 1398–1402 Vol.2. <https://doi.org/10.1109/ACSSC.2003.1292216>
- Andrew B. Watson and Albert J. Ahumada. 2011. Blur clarified: A review and synthesis of blur discrimination. *Journal of Vision* 11, 5 (09 2011), 10–10.
- Hugh R. Wilson and Douglas J. Gelb. 1984. Modified line-element theory for spatial-frequency and width discrimination. *J. Opt. Soc. Am. A* 1, 1 (1984), 124–131.
- Krzysztof Wolski, Daniele Giunchi, Nanyang Ye, Piotr Didyk, Karol Myszkowski, Radosław Mantiuk, Hans-Peter Seidel, Anthony Steed, and Rafał K Mantiuk. 2018. Dataset and metrics for predicting local visible differences. *ACM Transactions on Graphics (TOG)* 37, 5 (2018), 1–14.

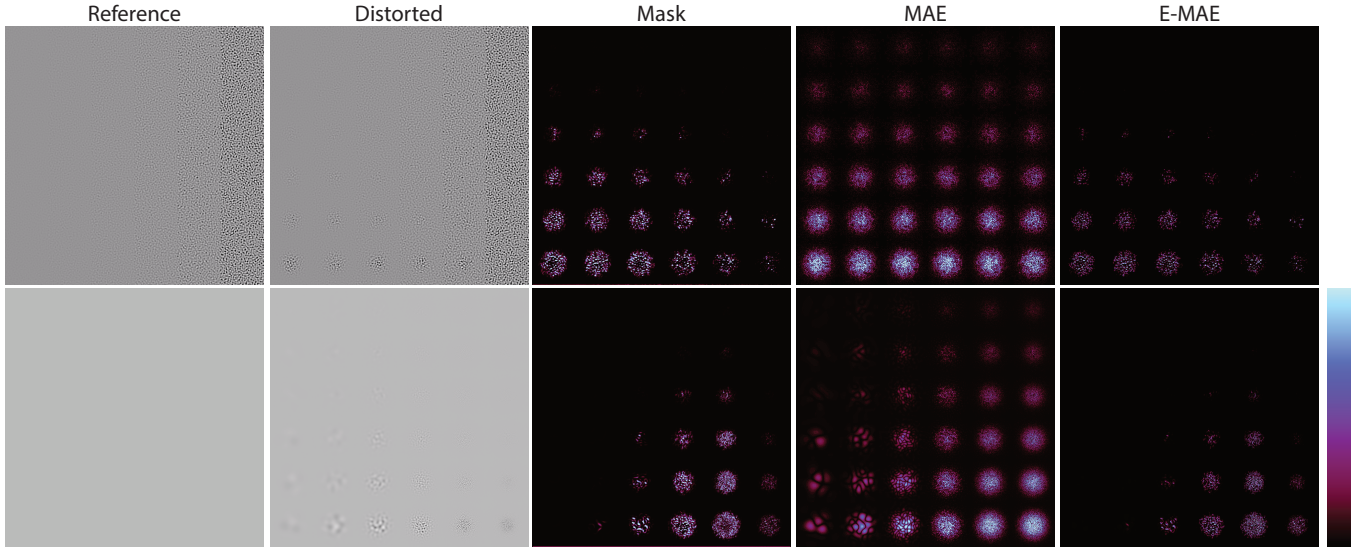


Figure 8: Error map prediction for the MAE and E-MAE metrics along with learned weighting masks for two perception patterns from [Čadík et al. 2013]. These patterns were specifically designed to investigate various perceptual phenomena, including contrast sensitivity and contrast masking. In the first row, the background consists of a high-frequency pattern with increasing contrast toward the right and a stimulus pattern with decreasing contrast from bottom to top (which becomes more apparent when zoomed in). In this scenario, contrast masking is more pronounced with increasing background contrast that in turn reduces the stimulus visibility, and E-MAE correctly predicts this effect. The second row presents another example, showing a set of patterns where their spatial frequencies increase toward the right while their contrast decreases toward the top. In this case, the learned masking roughly follows an inverse U-shape characteristic, akin to the contrast sensitivity function (CSF) [Daly 1993; Barten 1999; Wuerger et al. 2020]. Our masking well approximates the sensitivity drop for high frequencies but tends to suppress the visibility of low-frequency patterns excessively. In spite of this drawback, we still find it quite remarkable that the CSF shape becomes apparent in our learned mask without any explicit training with calibrated near-threshold CSF data.

Sophie Wuerger, Maliha Ashraf, Minjung Kim, Jasna Martinovic, María Pérez-Ortiz, and Rafal K. Mantiuk. 2020. Spatio-chromatic contrast sensitivity under mesopic and photopic light levels. *Journal of Vision* 20, 4 (04 2020), 23–23. <https://doi.org/10.1167/jov.20.4.23>

Syed Waqas Zamir, Aditya Arora, Salman Khan, Munawar Hayat, Fahad Shahbaz Khan, and Ming-Hsuan Yang. 2022. Restormer: Efficient transformer for high-resolution image restoration. In *Proceedings of the IEEE/CVF Conference on Computer Vision and Pattern Recognition*. 5728–5739.

Wenjun Zeng, Scott Daly, and Shawmin Lei. 2002. An overview of the visual optimization tools in JPEG 2000. *Signal Processing: Image Communication* 17, 1 (2002), 85–104.

Lin Zhang, Lei Zhang, Xuanqin Mou, and David Zhang. 2011. FSIM: A Feature Similarity Index for Image Quality Assessment. *IEEE Transactions on Image Processing* 20, 8 (2011), 2378–2386. <https://doi.org/10.1109/TIP.2011.2109730>

Richard Zhang, Phillip Isola, Alexei A Efros, Eli Shechtman, and Oliver Wang. 2018. The Unreasonable Effectiveness of Deep Features as a Perceptual Metric. In *CVPR*.

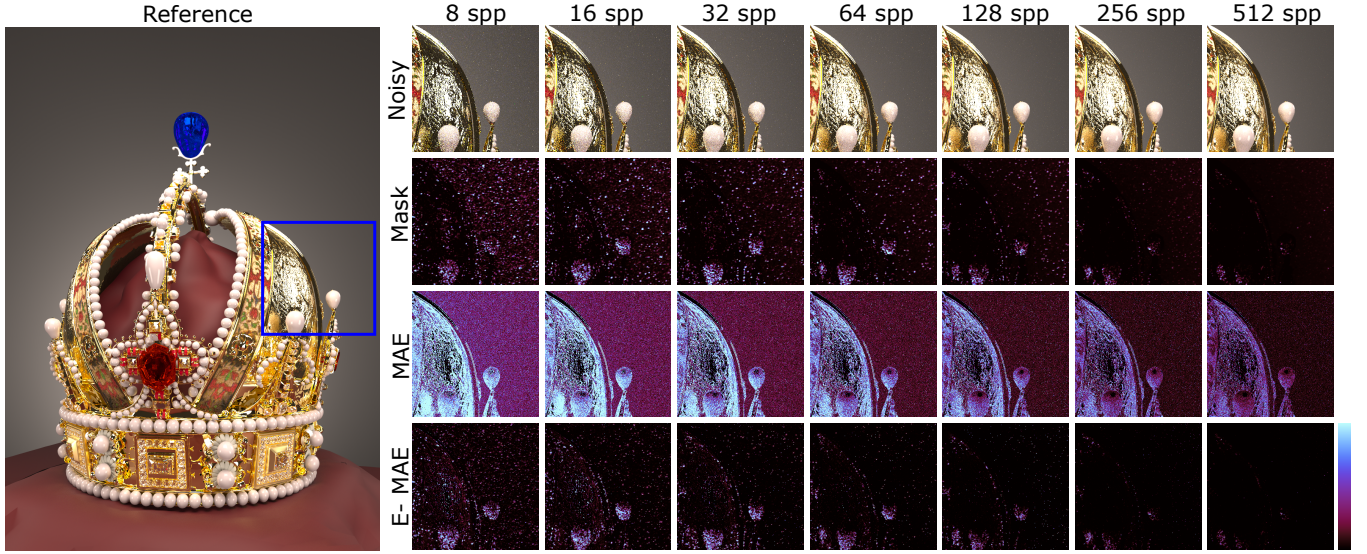


Figure 9: Our predicted masks and the resulting distortion maps as produced by our E-MAE metric for rendered images with varying numbers of samples per pixel (SPP). We also show the corresponding distortion map produced by the traditional MAE metric. As can be seen, the noise visibility is overestimated in the crown region while underestimated in the smooth background area, where it should be better visible due to limited visual contrast masking by the HVS. The reference image is rendered using 32k SPP. The test set has been introduced by Firmino et al. [2022].

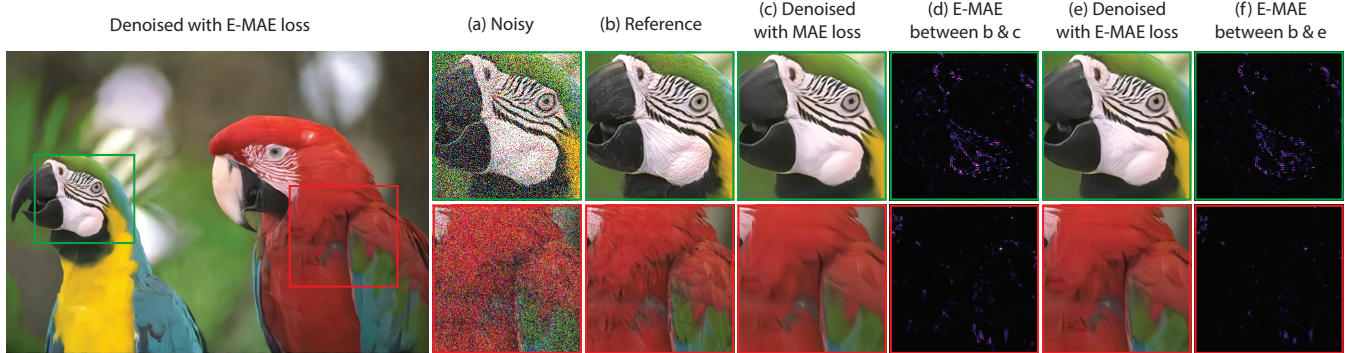


Figure 10: Visual results in the image denoising task when employing MAE and E-MAE as loss functions. Considering that denoiser networks typically reduce noise through smoothing, our objective was to investigate whether the use of the E-MAE loss could encourage the network to retain or hallucinate details, even if they do not precisely match the reference, still their discrepancy from the ground truth is not perceivable based on the E-MAE metric predictions. Although the denoised image with the E-MAE loss yields slightly sharper content or higher contrast, as evident from the comparison of E-MAE errors, the desired behavior of preserving details is not observed. It appears that the E-MAE is not sensitive to the level of blur caused by the denoiser network.

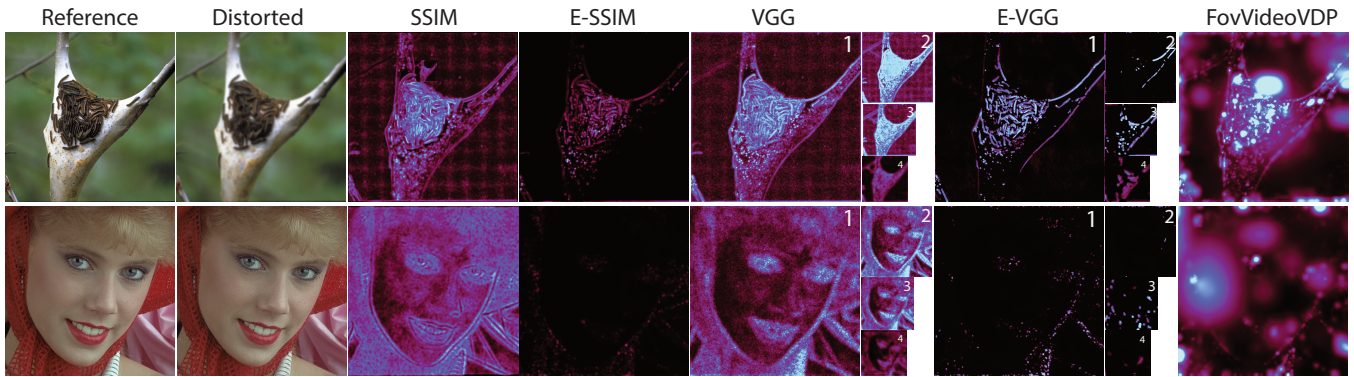


Figure 11: Error map visualizations for the SSIM and VGG metrics along with their enhanced versions (E-SSIM and E-VGG) and the FovVideoVDP metric [Mantiuk et al. 2021] for blur (top) and noise (bottom) distortions. Note that the SSIM values have been remapped to 1-SSIM, where lower values indicate less visible errors. For the VGG metric, we show the difference map for four different layers, which are obtained by averaging the difference maps of all channels within each layer.